Valley drift and valley current modulation in strained monolayer MoS_2

Nityasagar Jena, Dimple, Raihan Ahammed, Ashima Rawat, Manish Kumar Mohanta, and Abir De Sarkar*
Institute of Nano Science and Technology, Phase 10, Sector 64, Mohali, Punjab 160 062, India

(Received 17 June 2018; revised manuscript received 9 September 2019; published 21 October 2019)

Elastic-mechanical deformations are found to dramatically alter the electronic properties of monolayer (ML) MoS_2; particularly, the low-energy Bloch bands are responsive to a directional strain. In this study, in-plane uniaxial deformation is found to drift the low-energy electron/hole valleys of strained ML-MoS_2 far away from *K*/*K*' points in the Brillouin zone (BZ). The amount of drift differs notably from hole to electron bands, where the conduction band minimum (CBM) drifts nearly 2 times more than the valence band maximum (VBM) in response to a progressively increasing strain field (0–10%). The resulting strain-induced valley asymmetry/decoherence can lift the momentum degeneracy of valley carriers at the *K* point, thereby affecting the low-energy valley excitations (*K*-valley polarization) in a strained ML-MoS_2 lattice. The quantum origin of this decoherent valley arises from the differences in the Bloch orbital wave functions of electron and hole states at the exciton band edges and their deformation under strain. A higher drift (>1.5 times) is noticed when strain is along the zigzag (ZZ) axis relative to the armchair (AC) axis, which is attributed to a faster decline in Young's modulus and Poisson's ratio (PR) along the ZZ direction. A similar valley drift only in the VBM of uniaxially strained ML-MoS_2 was reported in an earlier local density approximation (LDA) based density functional theory (DFT) study [Q. Zhang *et al.*, Phys. Rev. B **88**, 245447 (2013)], where a massive valley drift occurring at the CBM was fully overlooked. Moreover, the giant VBM drift reported therein is 6 times the drift observed in our DFT studies based on spin-orbit coupling (SOC) and Perdew-Burke-Ernzerhof generalized gradient approximation (PBE-GGA) functionals. The physical origin of valley drift has been ascertained in our thorough investigations. The robustness of our approach is substantiated as follows. With progressive increase in strain magnitude (0–10%), the band gap remains direct up to 2% uniaxial tensile strain, under SOC, which accurately reproduces the experimental strain-induced direct-to-indirect band gap transitions occurring at ∼2% strain. Based on LDA-DFT [Q. Zhang *et al.*, Phys. Rev. B **88**, 245447 (2013)], this crossover in band gap has been incorrectly reported to occur at a higher value of uniaxial strain of 4%. Moreover, the direct SOC band gap shows a linear redshift at a rate of 51–53 meV/(% of strain), under uniaxial tensile strain, which is in excellent quantitative agreement with experimentally observed rates in the redshift of direct excitonic transitions measured in several optical absorption and photoluminescence (PL) spectroscopy experiments. In addition, the Berry curvature $\Omega(k)$ of electron/hole bands gets significantly modulated in strained ML-MoS_2, where the intensity of the flux profile increases as a function of the magnitude of strain with an opposite drift around *K*/*K*', when strained along the ZZ/AC direction. A strong strain-valley coupling leads to an enhancement in the strength of spin-orbit induced spin splitting of bands at VBM/CBM, which is sizably enhanced (∼7 meV) simply by the strain-controlled orbital motions. Our findings are of prime importance in the valley physics of MoS_2. Besides, the important theoretical insights emerging from this work will trigger further experimental investigations on ML-MoS_2 to realize its novel technological potential in nanoelectronics, spintronics, and valleytronics.

DOI: 10.1103/PhysRevB.100.165413

I. INTRODUCTION

Apart from a unit electric charge and discrete spin configurations, electrons in certain crystalline semiconductors acquire another valley pseudospin degree of freedom for their low-energy valley carriers due to the occurrence of multiple energy extrema in the electronic band spectrum [1]. Monolayer MoS_2 (ML-MoS_2) and other members of group-VIB transition-metal dichalcogenides (TMDCs), such as MX_2 (M = Mo, W and X = S, Se) have been a subject of intense focus in recent times due to their direct semiconducting band gaps (1–2 eV) and rich *d*-electron states [1,2]. While bulk MoS_2 is an indirect-gap semiconductor (∼1.29 eV) [3,4], a direct semiconducting band gap (∼1.8–1.9 eV) emerges at its two symmetry-inequivalent but energy-degenerate valleys (*K*/*K*'), when the bulk MoS_2 lattice is scaled down to its ultimate two-dimensional (2D) limit, i.e., single-layer MoS_2 [3,5]. In ML-MoS_2, the *K* and *K*' valleys are time-reversal partners and form a binary index in the low-energy electronic spectrum for valley-selective carrier excitations under a polarization selective photoexcitation [1,6]. The presence of unique high-symmetry valleys (*K*/*K*') and a strong spin-orbit coupling (SOC) endows this material with novel coupled spin-valley physics such as spin Hall and valley Hall effects [1,7]. The exotic chiral nature of valley carriers has been demonstrated in recent experiments, which can serve as a building block in future integrated spintronic and valleytronic

*Corresponding authors: abir@inst.ac.in; abirdesarkar@gmail.com

devices [6,8]. Additionally, the pristine surfaces of TMDCs devoid of any surface dangling bonds allow a facile integration with various substrates, and charge transport through them remains free from carrier localization or charge traps from surface roughness scattering, thereby leading to a high room-temperature mobility $\sim 200\,\mathrm{cm}^2\,\mathrm{V}^{-1}\,\mathrm{s}^{-1}$ in a top/bottom gated $HfO_2/MoS_2/SiO_2$ dielectric environment, where the current on/off ratios of a single-layer MoS_2 transistor can exceed (1×10^8) [9], which is ideal for next-generation low-power digital electronics.

In recent years, strain engineering of electronic structure has emerged as an efficient strategy to improve the performance of monolayer devices [10–13]. Elastic strain in MoS_2 has proved to reversibly modulate its tunnel resistance [14], charge carrier mobility [15,16], and optical absorption/emission efficiency to a large extent [11,17]. The unprecedented elastic tolerance of single- to few-layer-thick suspended MoS_2 nanosheets has been demonstrated in previous experiments, where an elastic deformation under a spherical nanoindenter (atomic force microscopy tip) reveals a surprisingly high average Young's modulus of 0.33 ± 0.07 TPa [18–20], which is 1/3 lower than the stiffness of free-standing graphene (1.0 TPa) [21], but higher than that of a freely suspended reduced graphene oxide (rGO, ∼0.25 TPa) [22]. A strong in-plane ionic (polar) covalent bonding in ML-MoS_2 [3] emanating from a strong overlap between $4d$ orbitals of molybdenum (Mo) and $3p$ orbitals of sulphur (S) [23] has enabled the sustenance of reversible dilation deformation in a strain range of 6–11%, where the critical breaking strength can exceed 23 GPa $(15 \pm 3\,\mathrm{N\,m}^{-1})$ [20,24,25]. Besides, ML-MoS_2 is insensitive to a lateral electric field in terms of its band gap modulation [26,27]. Thus, mechanical strain within the elastic bound turns out to be most effective strategy in tuning the band gap and optoelectronic response of a ML-MoS_2. The ease of applying mechanical strain reversibly in low-dimensional structures [17,28–30] and the alteration in optoelectronic properties with strain as a potential device have led to the emergence of straintronics [31–33], a new frontier in tailored nanoelectromechanics.

It is now well established that the electronic transport and optical excitations in a crystalline semiconductor (e.g. ML-MoS_2) are very much dependent on the characteristics of its electronic band dispersion, $E(k)$ and local curvature of bands (low-energy band topology) in the immediate vicinity of the Fermi energy (E_F) [13], where the conduction band minima (CBM) correspond to the excited states of electrons, while the valence band maxima (VBM) refer to the excited states of holes. Understanding the energy valley dynamics of these low-energy states in response to a symmetry lowering elastic deformation is of prime importance in strain engineering of a multivalley electronic material such as ML-MoS_2. Moreover, a simultaneous occurrence of strong spin-orbit coupling (SOC) and broken lattice inversion symmetry in ML-MoS_2 allows valley selective optical excitations between its time-reversed valley pairs (K/K'). It can be optically driven through helicity selective circularly polarized laser radiation, which causes excitonic excitations governed by its chiral optical valley selection rules (k-space valley physics) [1,6,8,34]. This opens up exciting possibilities to manipulate charge carriers in these time-reversed valley points with contrasting Berry-phase curvatures for electron/holes near the K/K' valleys (valley-Hall effects) [35]. Furthermore, valley and spin properties in these monolayers are closely related to their crystal symmetry and orbital wave functions at the energy band extremum [36]. Therefore, an alteration in these properties is expected under a symmetry-lowering uniaxial strain [37], similar to the experimental observation in an AlAs two-dimensional electron system [38].

In this work, the effects of in-plane lattice deformation on monolayer MoS_2 have been systematically investigated. The dynamics of low-energy valley states of electron and hole bands are found to differ distinctively in response to a directional strain perturbation, where the conduction band minimum (CBM) shows a pronounced drift relative to its valence band maximum (VBM). Furthermore, the energy-valley drift response is higher when strain is along the zigzag (ZZ) axis of MoS_2 as compared to the arm-chair (AC) axis. The underlying asymmetry is attributed to two physical effects brought about simultaneously by a symmetry-breaking strain: one is the geometric effect under a direction-dependent strain, which leads to an anisotropy in elastic constants, while the other one is the electronic effect due a changing orbital manifold and hybridization of states at the local band edges, i.e., CBM/VBM energy valleys. The asymmetry in the valley drift leads to an anomalous valley current in a strained MoS_2 lattice, where the Berry phase curvature distribution around the K point gets considerably modified under a direction-selective strain perturbation. Under extreme strain (∼10%), we also notice a non-negligible enhancement in the spin-orbit induced spin splitting of energy bands across the VBM and CBM of ML-MoS_2, around K and K' points, where a strong coupling between strain and spin degrees of freedom can manipulate the spintronic capability of this material.

II. COMPUTATIONAL DETAILS

Spin-polarized density functional theory (DFT) calculations have been performed based on projector augmented-wave (PAW) [39,40] pseudopotentials implemented within the plane-wave Vienna *ab initio* simulation package (VASP) [41–43]. Generalized gradient approximations (GGAs) for the exchange-correlation (XC) energy in its Perdew-Burke-Ernzerhof (PBE) [44,45] parametrization have been used to describe the electronic wave functions in a plane-wave basis set. The electronic and ionic relaxation was based on the conjugate-gradient (CG) algorithm with a kinetic energy cut-off of 520 eV and a Γ-centred $16 \times 9 \times 1$ k mesh for the Brillouin- zone (BZ) integration. The valence electronic configurations for Mo and S atoms are $4p^6 5s^1 4d^5$ and $3s^2 3p^4$, respectively. Energy tolerance for the total energy convergence in a self-consistent iteration was set to 1.0×10^{-8} eV, where the individual atoms are allowed to relax until the magnitude of Hellmann-Feynman forces acting on each atom reaches less than $1.0 \times 10^{-3}\,\mathrm{eV/Å}$. The periodic slabs in the supercell were decoupled by considering a large vacuum spacing >14 Å (the dimension of the supercell along the c axis was >18 Å). Furthermore, dipole corrections have been incorporated to eliminate the spurious dipolar interactions between the periodic replicas of slabs along the direction perpendicular to the surface of ML-MoS_2. Fully relativistic spin-orbit

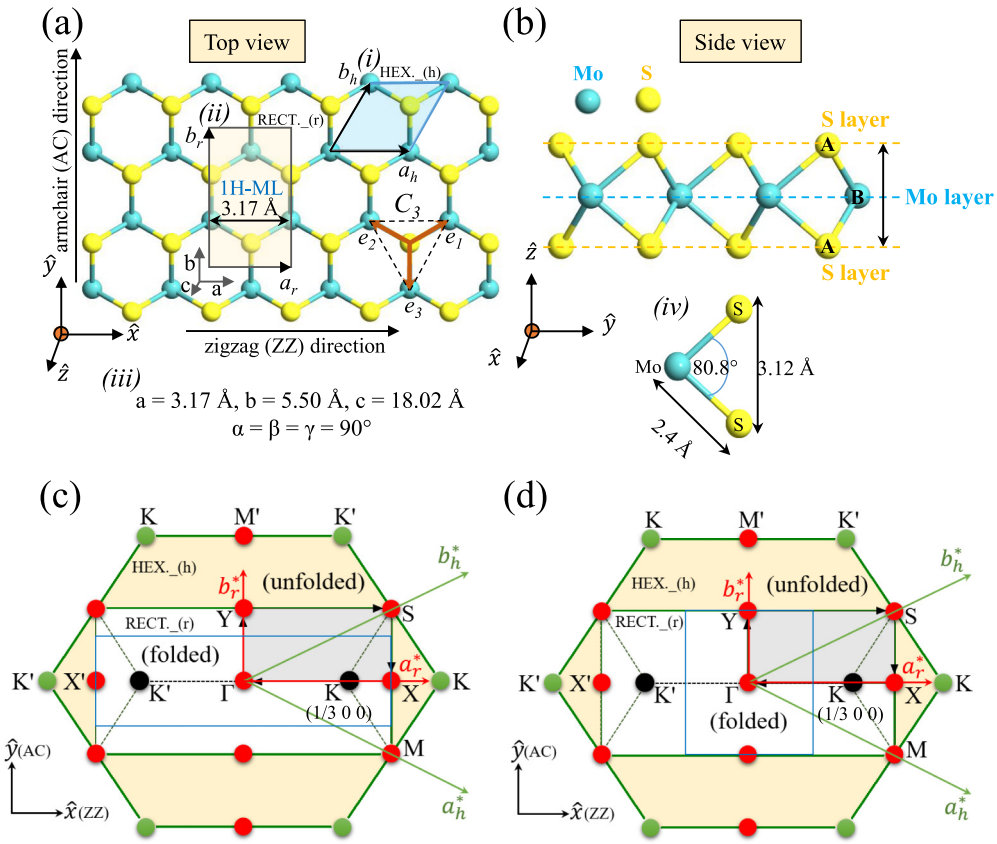

FIG. 1. (a) A top view schematic of monolayer (ML) MoS_2: (i) optimized geometry in primitive hexagonal unit cell, and (ii) rectangular supercell with lattice parameters presented in panels (iii) and (iv), respectively. The lattice vectors for hexagonal and rectangular cells are $\mathbf{a}_h$, $\mathbf{b}_h$ and $\mathbf{a}_r$, $\mathbf{b}_r$, respectively, whereas, $\mathbf{e}_1$, $\mathbf{e}_2$, $\mathbf{e}_3$ are the nearest neighbor vectors about a C_3-rotation axis centered over the S atom in a Mo-S trigonal-prismatic coordination. (b) A side view schematic of ML-MoS_2 with an A-B-A type trilayer S-Mo-S atomic packing. The dashed blue line in (b) over the central Mo layer is an indicator of the plane of mirror symmetry (σ_h) in broken inversion symmetric ML-MoS_2. (c)–(d) A schematic representation of the 2D unfolded hexagonal Brillouin zone (BZ) (yellow filled region) and folded rectangular BZ (white filled region) for a primitive hexagonal and orthorhombic supercell superimposed with relevant high-symmetry k points.

coupling (SOC) effects were considered for the self-consistent ion relaxation of strained geometries. The Berry curvatures were calculated with SOC effects turned on using the methods discussed in Ref. [46].

III. RESULTS AND DISCUSSION

A. Strain geometry and Brillouin zone folding

A honeycomb lattice structure of monolayer (ML) MoS_2 was composed of covalently bonded triatomic planes of S-Mo-S atoms with a transition-metal (Mo) layer sandwiched between two staggered hexagonal sublattices of chalcogen (S) in an ABA Bernal stack sequence, as schematically represented in Figs. 1(a) and 1(b). An orthorhombic supercell was constructed for the purpose of applying strain independently along two of the most relevant crystallographic orientations of MoS_2, namely, the zigzag (ZZ) and armchair (AC) directions [33]. The inherent hexagonal symmetry of MoS_2 is retained in an orthorhombic supercell upon geometry optimization, where the input experimental bulk lattice constant, $a = 3.16$ Å ($d_{\mathrm{Mo-Mo}}$) for a primitive hexagonal unit cell, converges to $a = 3.17$ Å ($d_{\mathrm{Mo-Mo}}$), $b = 5.50$ Å for an orthorhombic supercell, shown in Fig. 1(a)-(ii). The optimized lattice parameters shown in Figs. 1(a) and 1(b) are in very close agreement with earlier numerical results using similar exchange-correlation functionals and supercell symmetry [47,48]. Investigations reported herein are based on an orthorhombic supercell.

The BZs of our unstrained system have been constructed by a proper folding of its hexagonal Brillouin zone (yellow filled region) into a rectangular zone (white filled region), as shown in Figs. 1(c) and 1(d), where the high-symmetry K point of a hexagonal BZ is folded into the midpoint of the line connecting K and Γ (in the hexagonal BZ), i.e., the symmetry point K (1/3 0 0) (black dot), located at a 2/3 length of the Γ-X high-symmetry line in a rectangular BZ [49,50]. The blue rectangular line inside of folded rectangular BZ in Figs. 1(c) and 1(d) shows the first BZ of strained MoS_2 when strain is along its ZZ/AC direction in an orthorhombic supercell.

B. Impact of strain on low-energy valleys of ML-MoS_2

Figure 2(a) shows the energy-momentum dispersion, E(k) of strain-free monolayer MoS_2 in an orthorhombic supercell. Without explicit inclusion of the spin-orbit coupling (SOC) effect, a direct semiconducting band gap, $E_g(K\text{-}K) \sim 1.69$ eV, occurs along the X-Γ high symmetry line, where the band

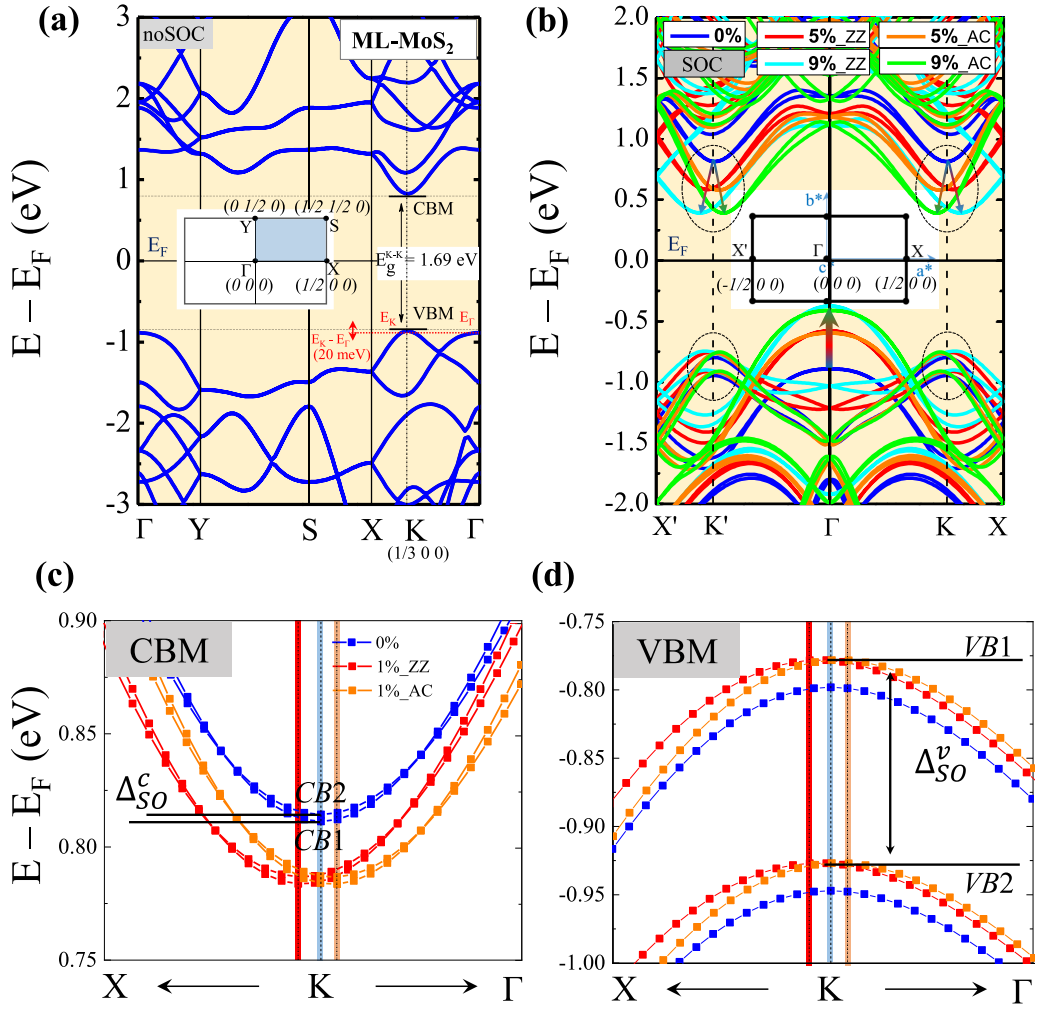

FIG. 2. (a) The band structure of strain-free ML-MoS_2 in an orthorhombic supercell shows a direct semiconducting band gap, $E_g = 1.69$ eV (without SOC), along the X-Γ high-symmetry line. (b) Evolution in the band structure of unstrained (0%) and uniaxially strained (5%, 9%) ML-MoS_2 along the ZZ/AC direction. The CBM valleys near K/K' show a strong strain-dependent momentum drift over the valence band hills. The band structure shown in (b) includes the effect of SOC. (c)–(d) Low-energy spin-split conduction band minima (CB1, CB2) and valence band maxima (VB1, VB2) around the K point, when ML-MoS_2 is strained by 1%. The CBM/VBM valleys drift along the opposite direction in response to lattice strain along the ZZ/AC direction. The vertical color bars represent the position of energy band top or bottom.

extrema of electron/hole states lie over a single folded K point (1/3 0 0), positioned at 2/3 of the length of the Γ-X line. The highest occupied states (VBM) occurring at E_K and that lying at a slightly lower energy (∼20 meV offset) E_Γ show excellent agreement with previous theoretical results using a similar level of DFT methodology [51,52].

Next, uniaxial tensile strain in a dilation deformation range of 0–10% was applied along both the ZZ as well as AC directions of ML-MoS_2. The evolution in the band dispersion and curvature of bands around the Fermi energy (E_F) within an energy range of $E(k) \pm 2$ eV is shown in Fig. 2(b). We find a strong strain-valley coupling between low-energy Bloch bands and mechanical strain near the CBM/VBM band edges, where an applied uniaxial deformation significantly drifts around the CBM valleys and VBM hills far away from K/K' points in the momentum space, as shown in Fig. 2(b) (see Fig. S1 in the Supplemental Material for continuous evolution from 0% to 10% strain [53]). This arc-shaped drift response is found to be stronger in the electron sector of band dispersion than the hole sector, with several band extrema crossing around K and K' point for different values of uniaxial strain. In the limit of a small strain of 1%, in Figs. 1(c) and 1(d) we have shown the energy valley drift in the lowermost spin-split conduction band (CB1, CB2) and the uppermost valence band (VB1, VB2). The parabolicity of electron subbands gets more heavily deformed than the hole bands with energy vertices crossing around the K point, when strained along the ZZ/AC axis [see Figs. 1(c) and 1(d)]. The curvature distortion can introduce particle-hole asymmetry due to a nonidentical band dispersion around the K point [13,23]. Microscopically, the origin of this strong strain-valley coupling is due to a changing geometric effect that reduces the symmetry of the underlying lattice and a changing orbital hybridization effect (wave-function overlap effect) for relevant local Bloch states at the CBM/VBM band edges. A strain-induced modification in the band-edge orbital wave functions generate a scalar

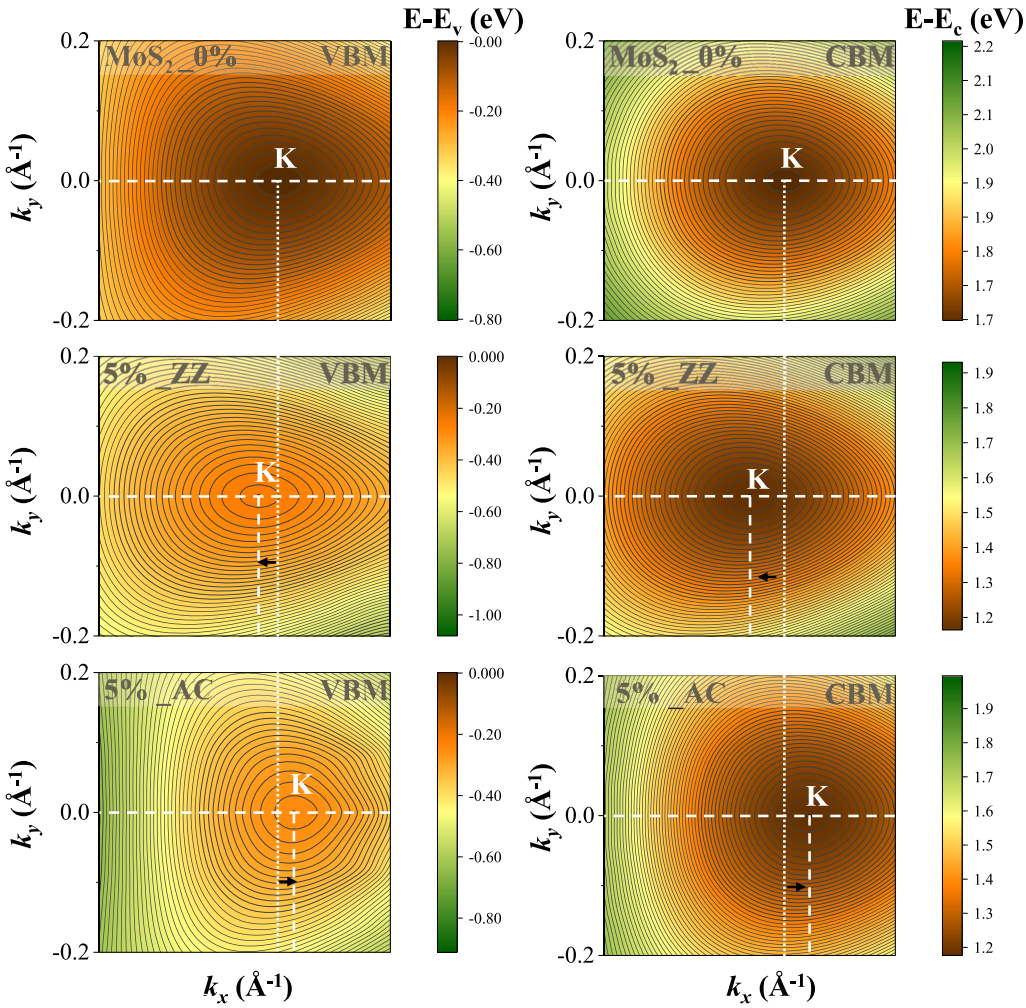

FIG. 3. Isoenergy contours of low-energy valence and conduction bands in a 2D k plane for unstrained (0%) and 5% strained ML-MoS_2 along the ZZ/AC direction. The dashed line and arrows illustrate the energy valley drift near the K point. This energy contour feature is also true for its symmetry inequivalent K' point due to time-reversal symmetry. The VBM/CBM constant energy contours have been scaled with respect to the energy of the valence band top and conduction band bottom at the K point. Under strain we see a strong effect of trigonal warping (TW) of energy bands near the K point, where the energy valleys drift along opposite directions under ZZ/AC strain.

potential of varying strength for corresponding Bloch bands that are described by the low-energy electron and hole valleys of a monolayer MoS_2. A detailed discussion has been provided in the next subsection, C.

To make this energy valley drift more evident, in Fig. 3 we present the constant energy contours of highest occupied (VBM) and lowest unoccupied (CBM) bands near the K point. Unlike graphene, the VBM/CBM isoenergy contours of monolayer MoS_2 are not isotropic in close proximity of the K point, and a trigonal warping (TW) effect of energy bands can be seen in the equienergy lines around the K point (this feature is also true for energy vertices around the K' point, as a consequence of time-reversal symmetry in the system) [54,55]. When uniaxially stained (5%), an increase in the warping effect distorts the isoenergetic lines around the energy valleys due to a continuous reduction in threefold planar rotational symmetry (C_{3v}) and translational symmetry along its mutually perpendicular lattice directions. The TW effect is more pronounced at a larger k, and increases with an increasing strain field with an antisymmetric warping strength, when strain is along the ZZ/AC direction. In the immediate proximity of K, the hole surface is more strongly warped than the electron, where the low-energy contours of a strained system (along the ZZ direction) show an elliptic warping of band topology extending to a much higher energy with flattening of convexity revolution around the K point along the direction of applied strain, while it is closer to a triangular shape along the AC direction. The uniaxial strain-induced anisotropy in electronic band dispersion (trigonal warping effect) Coulomb drags the charge carriers anisotropically due to a strong interparticle-particle correlation that lead to an anisotropy in carrier mass/carrier mobilities and optical anisotropy in absorption coefficient as seen in our previous strain-engineering studies [24,56]. The CBM drift is larger than the VBM hills, with energy valleys drifting along opposite directions, when strained along the ZZ/AC direction.

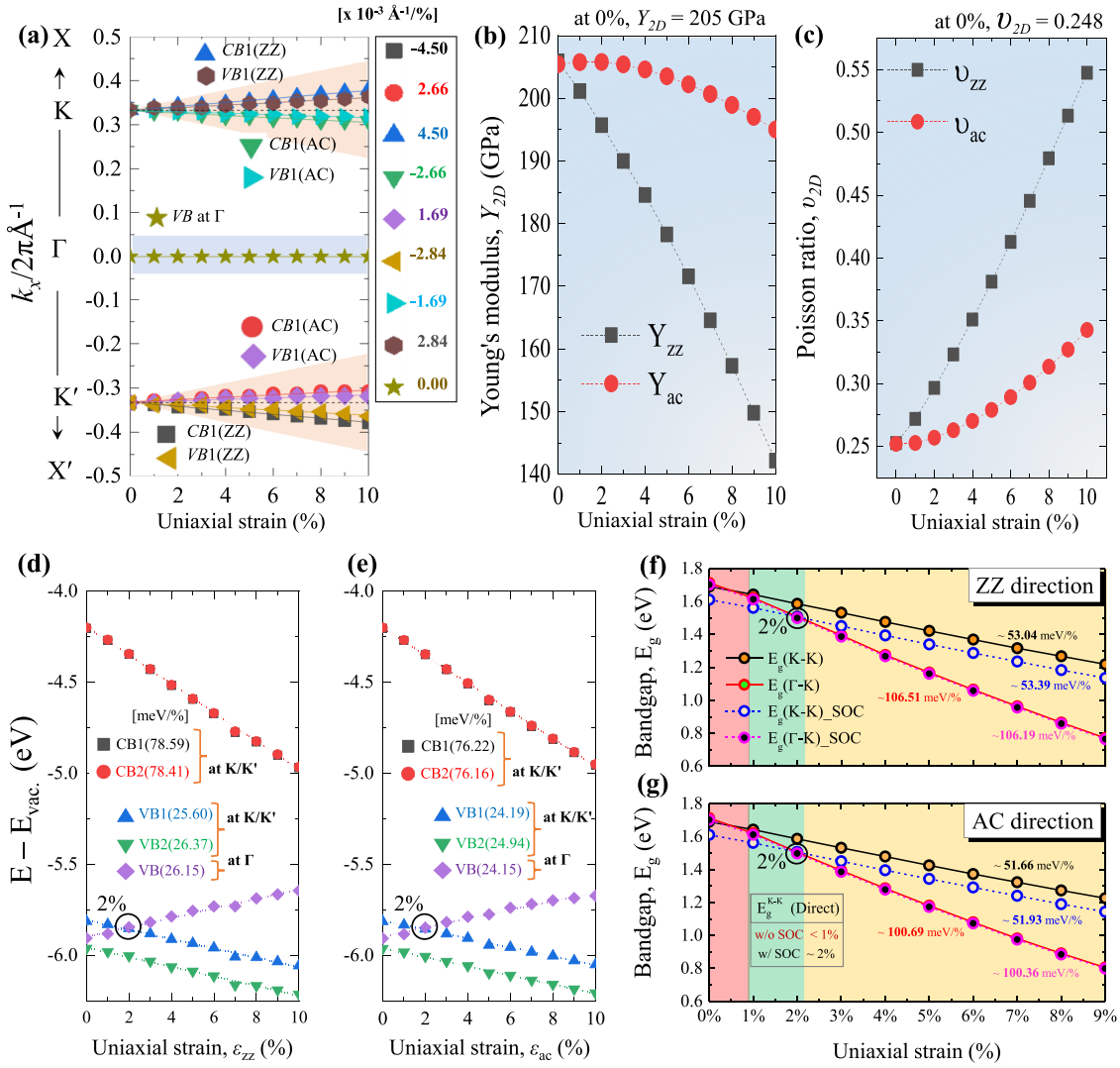

FIG. 4. (a) Momentum drift in the lowermost spin-split conduction band (CB1) and uppermost valence band (VB1) at *K*/*K*' points as a function of uniaxial strain along the ZZ/AC direction in a strain range of 0–10%. Variation in Young's modulus (b) and Poisson's ratio (c) with strain. A strong strain-dependent anisotropy in elastic parameters can be seen in (b) and (c), when strain is along its ZZ/AC direction. (d)–(e) Functional relationship of band-edge deformation energy with uniaxial strain applied along the ZZ/AC direction. CB1, CB2 are the spin-split conduction band minima (CBM) and VB1, VB2 are the spin-split valence band maxima (VBM) near the *K*/*K*' point, while VB is the spin-degenerate valence band top at the Γ point. The bracketed numbers are their variation rates in units of meV/strain%, with energy referenced to the absolute vacuum energy ($E_{vac.}$). (f)–(g) Variation in the direct, E_g(*K*-*K*) and indirect, E_g(Γ-*K*) band gaps with uniaxial tensile strain (0–10%) along the ZZ/AC direction, with (w/) and without (w/o) explicit inclusion of spin-orbit coupling (SOC) effects into the band structure calculation. The red and green shading in (f) and(g) is the strain range for direct-to-indirect band-gap crossover w/o and w/ SOC effects turned on.

This observation is in line with the result of our band structure calculation presented in Fig. 2(b).

In the following, we quantify the energy valley drift in the lowermost spin-split conduction band (CB1) and uppermost valence band (VB1). We further study the band-edge deformation energies of spin-split CBM (CB1, CB2) and VBM (VB1, VB2) and, concurrently, the changes in elastic constants such as Young's modulus, the Poisson ratio, and band-gap variations with strain, as the SOC is turned off or on. The changes in the above-mentioned quantities have been analyzed in a strain range of 0–10% along the ZZ as well as AC direction.

Uniaxial strain, which gets applied asymmetrically along a given crystal axis (ZZ/AC direction), reduces the original hexagonal symmetry in ML-MoS_2 about a C_3 rotation axis. As a result, both the translational symmetry and rotational symmetry are broken due to asymmetric Mo-S bond stretching [37]. As shown in Fig. 4(a), the lowermost spin-split CBM (CB1) drifts off the *K*/*K*' point at a rate (CB1/ZZ) $\sim 4.50 \times 10^{-3}$ Å^{-1}/1% when strain is along the ZZ direction, while it drifts towards the zone-center (Γ) at a rate (CB1/AC) $\sim 2.66 \times 10^{-3}$ Å^{-1}/1% when strain is along the AC direction. We find, the energy valley drift in spin-split

CB1 is higher (>1.5 times) along the ZZ direction than the corresponding drift along its AC direction. The momentum drift rates are found to be equal in magnitude at K and K' but of opposite nature in their slopes. A similar drift response is found for the valence band hills, where the uppermost spin-split valence band top (VB1) drifts away from K/K' at a rate (VB1/ZZ) $\sim 2.84 \times 10^{-3}$ Å^{-1}/strain % when strain is along the ZZ direction, while it drifts towards the zone center (Γ point) at a rate (VB1/AC) $\sim 1.69 \times 10^{-3}$ Å^{-1}/strain % when strained along the AC direction.

A higher drift in momentum-space for both CB1 and VB1, when applied strain is along the ZZ direction is attributed to a drastic change in elastic constants, such as Young's modulus (Y) and Poisson ratio (υ), as shown in Figs. 4(b) and 4(c). A significant drop in the Poisson ratio along its ZZ lattice direction has a profound effect on the Brillouin zone deformation, which scales linearly with strain applied along the ZZ direction.

Valley drift shows a large strain dependency. The CBM valley drift is nearly two times the drift in its VBM hill. Consequent to the application of uniaxial strain, the electron/hole valleys at K or K' points no longer coincide. As a result, the valley symmetry between excitons (valley coherence) gets destroyed due to a strong strain-induced electron-hole valley asymmetry near the K point. Since valley degrees of freedom in ML-MoS_2 emerge from its local band extrema, the drift could soften the valley-selective optical selection rules due to changes in the optical matrix elements and excitonic wave functions, which in turn can have profound effects on intervalley optical excitations and electron dynamics due to radiative dephasing of carriers in a strained ML-MoS_2 lattice. This uniaxial strain-induced valley asymmetry in the vicinity of transition point (K/K') could possibly be the reason for a drastic reduction in the degree of circular polarization (K-valley polarization) in uniaxially strained ML-MoS_2 in the experimental observation led by Zhu *et al.* [37] in a polar photoluminescence (PL) emission measurement, where the degree of valley polarization gets reduced with increase in strain magnitude. It is worth noting here that, although the low-energy valleys of strained ML-MoS_2 show a strong momentum-dependent valley drift around K/K' points, no energy difference between K and K' is observed, i.e., the energy degeneracy in the symmetry inequivalent valleys of strained ML-MoS_2 is retained even up to a large uniaxial strain of 10%. This shows that elastic uniaxial deformation alone (without a real external magnetic field) is not sufficient to lift the valley energy degeneracy between K and K' by a strain-induced fictitious gauge-field vector potential (which generates a uniform pseudomagnetic field) due to its time-reversal-invariant (TRI) nature. However, a pure shear strain which induces a spatially varying strain field can lift the valley degeneracy in transition-metal dichalcogenide monolayers including ML-MoS_2 [57], similar to the observed phenomenon in a nonuniformly shear strained monolayer graphene [58].

Figures 4(d) and 4(e) track the subband energy evolution (band-edge deformation potentials) of spin-split conduction band minima (CB1, CB2) and valence band maximum (VB1, VB2) as a function of uniaxial strain. VB lies at the edge of the spin-degenerate valence band at the Γ point. ML-MoS_2 shows a direct gap with CB1 and VB1 coinciding at the K point. When influenced by a uniaxial deformation, the spin-split CBM (CB1, CB2) at the K/K' point show a stiff energy variation at a rate 76–78 meV/% due to a strong out-of-plane character of Mo $4d_{z^2}$ orbital states, when strain is along the ZZ/AC direction, while the spin-degenerate VBM (VB) at Γ point varies at a rate (24–26 meV/%) with a valence band crossover occurring at 2% strain. On the other hand, the spin-split VB1, VB2 exhibit a smaller energy shift at a rate 24–26 meV/strain % due to the pure in-plane nature of Mo $4d_{xy} + 4d_{x^2-y^2}$ orbitals which gets weakly influenced by an in-plane strain. Figures 4(d) and 4(e) shows the band-edge deformation potential to be highly strain tunable for low-energy Bloch bands having out-of-plane orbital character (i.e., CBM at K).

Figures 4(f) and 4(g) show the energy evolution in the direct (K-K) and indirect (Γ-K) band-gap energies (E_g), with (w/) and without (w/o) explicit inclusion of SOC effects. Inclusion of SOC effects lead to a giant spin splitting at VBM (VB1, VB2) that reduces the direct band gap in ML-MoS_2 by 80 meV (w/o SOC, $E_g \sim 1.69$ eV; w/ SOC, $E_g \sim 1.61$ eV) [59] while keeping the band edges at the K point, where the spin-split valence band top VB1 shifts up in energy by an amount 57.2 meV and VB2 shifts down by 92 meV with respect to the spin-degenerate valence band (w/o SOC) at the K point. An energy separation of 149.3 meV between spin-split VB1 and VB2 in our calculation shows very close agreement with experimentally measured values for strain-free monolayer MoS_2 (146 meV) [29] and a numerical calculation reporting a value of 148 meV [60]. The valence band energy offset between E_K and E_Γ increases by a factor of 4 under SOC (~92.58 meV) with respect to the energy offset w/o SOC (~20 meV), which is much higher than the room temperature thermal energy (~26 meV). This important feature in the band structure of ML-MoS_2 has not received much attention, but it moves the critical strain limit to ~2% for a direct-to-indirect band-gap crossover. Our theoretical calculation shows excellent quantitative agreement with several experimental observations where the direct-to-indirect band-gap transition in ML-MoS_2 occurs at a critical strain strength of ~2% [12,17,61], whereas without SOC this crossover in band gap occurs at <1% of lattice strain due to a relatively small energy offset (~20 meV) between occupied bands. This also agrees with the numerical results, where the SOC effects have not been explicitly included in the band structure calculation [51,52]. The VBM energy at the Γ point is found to be lower by 14 meV under SOC than that of w/o SOC. In Figs. 4(f) and 4(g), for all cases the band gap decreases monotonically with increasing strength of uniaxial strain, maintaining a nearly linear redshift in energy gaps. The redshift rate in the direct band gap is $E_g(K\text{-}K)$ ~ 53 meV/(% of strain) along the ZZ direction and $E_g(K\text{-}K) \sim 51$ meV/(% of strain) along the AC direction. The redshift rates with and without inclusion of SOC effect show excellent quantitative agreement with experimentally observed redshift rates in the direct-gap optical transition energies: ~35 meV/1% strain [62], ~45 ± 7 meV/% [17], and ~48 meV/(% of strain) [37] measured in several optical absorption and photoluminescence (PL) measurements.

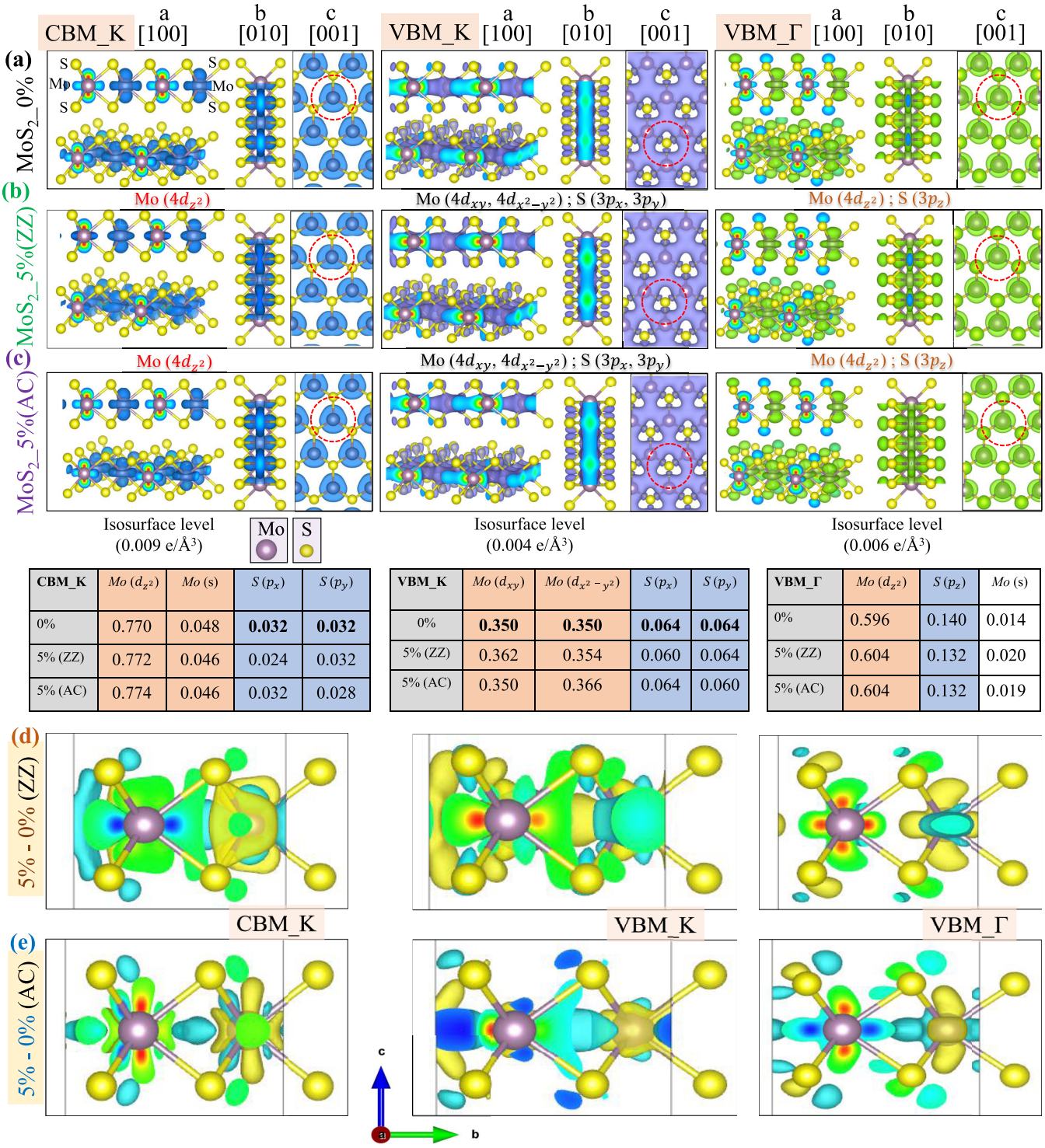

CBM_K	*Mo* (d_{z^2})	*Mo* (s)	*S* (p_x)	*S* (p_y)
0%	0.770	0.048	**0.032**	**0.032**
5% (ZZ)	0.772	0.046	0.024	0.032
5% (AC)	0.774	0.046	0.032	0.028

VBM_K	*Mo* (d_{xy})	*Mo* ($d_{x^2-y^2}$)	*S* (p_x)	*S* (p_y)
0%	**0.350**	**0.350**	**0.064**	**0.064**
5% (ZZ)	0.362	0.354	0.060	0.064
5% (AC)	0.350	0.366	0.064	0.060

VBM_Γ	*Mo* (d_{z^2})	*S* (p_z)	*Mo* (s)
0%	0.596	0.140	0.014
5% (ZZ)	0.604	0.132	0.020
5% (AC)	0.604	0.132	0.019

FIG. 5. Bloch states at various k points, orbital wavefunction of electronic states at the vertices of the conduction band valley (CBM_K), and valence band hills (VBM) located at K and Γ points for strain-free (a), and 5% strained ML-MoS_2 along the zigzag (b) and armchair (c) directions. The orbital structure of Bloch states is projected from different crystallographic viewpoints with their orbital character labeled therein. The charge density isosurfaces have the same isolevel along a particular column in (a)–(c) in units of $e/\text{Å}^3$. The table summarizes the orbital composition of Bloch states at the band edges of CBM/VBM. (d)–(e) Difference in Bloch wavefunction along the ZZ/AC direction for relevant edges at an isosurface level of $0.6 \times 10^{-3}\, e/\text{Å}^3$. A strong delocalization effect can be seen when strain is along the ZZ direction.

Moreover, the redshift in their indirect band gap, $E_g(\Gamma\text{-}K) \sim 100\,\text{meV}/\%$, is in good accord with its theoretical value 94.6 ± 2.2 meV/% [61]. The energy band-gap redshift rate is slightly higher along the ZZ direction as compared to the AC direction, attributed to a faster decline in elastic constants along the ZZ direction, which seems to be the elastically soft direction in ML-MoS_2 with respect to its relatively stiff AC direction [see Figs. 4(b) and 4(c)].

A similar valley drift only in the VBM of uniaxially strained ML-MoS_2 has been reported by Zhang *et al.* [63], where a 4% uniaxial tensile strain was applied along the ZZ direction of ML-MoS_2 by changing the direction of applied strain from 0°, 15° to 30°. A related observation in the Dirac cone drift of a uniaxially strained graphene sheet (strain = 2%, angle = 0°, 20°) has been reported by Mohr *et al.* [54] In their predictive findings, Zhang *et al.* [63] have shown a giant VBM drift in ML-MoS_2 (about the K point) to be 12 times that of the Dirac cone drift in graphene. However, Zhang *et al.* [63] remained silent about a massive drift occurring in its CBM both at K and K' points. In contrast, in our current study, we find the drift in the CBM to be nearly 2 times the observed valley drift in the VBM in a uniaxial strain range of 0–10%.

On the other hand, the valence band drift along the ZZ direction observed in our study is 1/6 the drift reported by Zhang *et al.* [63] using almost the same lattice constant (3.17 Å) of ML-MoS_2. However, the calculation approach significantly differs in the choice of different exchange-correlation functionals (PBE-GGA) and lattice strain range, 0–10%. The choice of the local density approximation (LDA) in their study poorly determines the band gap and critical strain range for direct-to-indirect band-gap crossover, where the directness of the band gap remained up to a higher value (∼4%) of uniaxial strain along the ZZ direction [63]. Several experimental and theoretical studies on ML-MoS_2 suggests the direct-to-indirect band-gap crossover would occur at nearly 2% of strain [12,17,29,33,37,61,64,65], as found in our DFT study. Moreover, using the more accurate *GW* correction to the quasiparticle (QP) band structure, Hongliang *et al.* [12] have shown ML-MoS_2 to remain a direct gap semiconductor at 1% tensile strain, and it becomes an indirect-gap semiconductor at 3% of tensile strain with a crossover in the band-gap type occurring between 2% and 3% of strain, which is close consistent with our PBE-SOC results.

Moreover, in Fig. 2, Zhang *et al.* [63] have shown the drift in the valence band top near the K/K' points (they use K_1/K_2). The valence band top in their magnified Fig. 2(b) [63] shows an abrupt change in band topology about the K point along the lines $\Gamma K_1 M_1 \Gamma$ (red dashed line) and $\Gamma K_2 M_2 \Gamma$ (green dashed line). This hump-like feature is quite unphysical for the studied system, and the local curvature of bands around K_1 and K_2 points has to be equal and opposite both for electron and hole sectors of bands in correspondence to the time-reversal symmetry in the system. But they find the VBM along the Γ-K_1-M_1-Γ path to drift off the K point, whereas along the Γ-K_2-M_2-Γ path it is still located exactly at the K point in Fig. 2(b) of their report, which is counterintuitive and not true.

In short, the calculation approach in our study is robust and more suitable for an accurate valley drift study along the most relevant crystallographic orientations of ML-MoS_2 rather than a constant strain applied along the arbitrarily chosen lattice directions. Furthermore, Zhang *et al.* [63] suggested the changes in band gap E_g to be more sensitive to the magnitude of applied strain rather than its angle. Hence, the magnitude of applied strain within the elastic bound (0–10%) has more practical relevance as conducted in our study.

We have also explored shear and biaxial strain modes. Due a relatively low elastic bound of shear strain ∼5–6%, we have not considered this as our main discussion [24]. However, interestingly, even at a high value of shear strain ∼5%, the band gap remains direct at K/K' (see Fig. S3(a) of the Supplemental Material [53]). Priya Johari *et al.* [64] attribute this to the inability of shear strain to delocalize the electronic charge density isosurfaces of MoS_2, while the biaxial strain mode has no effect on valley degeneracy lifting due to the isotropic nature of the strain field that preserves the symmetry of underlying crystal (see Fig. S3 (b) of the Supplemental Material [53]).

C. Strain effect on Bloch orbitals at band edges

Apart from a strain-induced geometric effect that reduces the symmetry of a hexagonal lattice, another microscopic physical effect underlying energy valley drift is the asymmetry in the orbital overlap of electronic states under a symmetry-breaking lattice displacement. In Figs. 5(a)–5(c), we have carefully mapped the orbital wavefunctions of relevant band-edge states that describe the low-energy electron and hole dispersion of a pure and strained ML-MoS_2 lattice. The orbital wave functions at the band edges are primarily composed of 4d orbitals of Mo and 3p orbitals of S with a dominance of d character in electronic states. In ML-MoS_2, the trigonal-prismatic crystal field on Mo 4d orbitals lifts the fivefold degeneracy of free Mo d orbitals into three energy groups, which spread out in energies, giving rise to two doubly degenerate energy levels (i) $4d_{xy}$, $4d_{x^2-y^2}$ and (ii) $4d_{yz}$, $4d_{zx}$ and one singly degenerate energy level (iii) $4d_{z^2}$ [66]. The in-plane $4d_{xy}$, $4d_{x^2-y^2}$ orbitals and the out-of-plane $4d_{z^2}$ orbitals are symmetric with respect to its horizontal mirror plane (σ_h) lying over the Mo atomic layer. The out-of-plane mirror symmetry ($z = -z$) in ML-MoS_2 allows hybridization between its $4d_{xy}$, $4d_{x^2-y^2}$, and $4d_{z^2}$ orbitals with $3(p_x,\ p_y)$, $3(p_z)$ orbitals of ligand sulfur (S) atoms, which opens up a tunable energy gap at its two symmetry inequivalent K/K' valleys.

The CBM of a strain-free ML-MoS_2 mainly originates from the mixing of $4d_{z^2}$ orbitals of Mo with $3(p_y + p_x)$ orbitals of sulfur (S). A small contribution also arises from Mo 5s orbitals. The bandwidth analysis of each contributing orbital to the relevant band-edge states is summarized in a table in Fig. 5, which shows that each Mo atom contributes a total of 92% spectral weight to its CBM antibonding state, while each S atom puts in 4%. The VBM states at the K point are constructed by a linear combination of doubly degenerate $4(d_{xy} + d_{x^2-y^2})$ bonding orbitals of Mo, with an orbital weight of 42%, contributed in equal proportion hybridized with sulfur $3p_y$ and $3p_x$ orbitals each contributing 3.8% of spectral weight. A vanishing contribution to VBM (at K) also arises from Mo $4p_y$ and $4p_x$ orbitals, each having 0.2% spectral weight. The nearby valence band tops at the Γ point (VBM_Γ), resulting from the hybridization of Mo ($4d_{z^2}$) orbitals with antibonding $3p_z$ orbitals of S, each contribute 79% and 9.3%, respectively, with weakly contributing 5s and 3s orbitals of Mo and S atoms.

Under the application of uniaxial strain, the bandwidths of the contributing orbitals show a pronounced change which arises due to a change in the crystal field splitting between metal and ligand (Mo-S) in the trigonal prismatic coordination

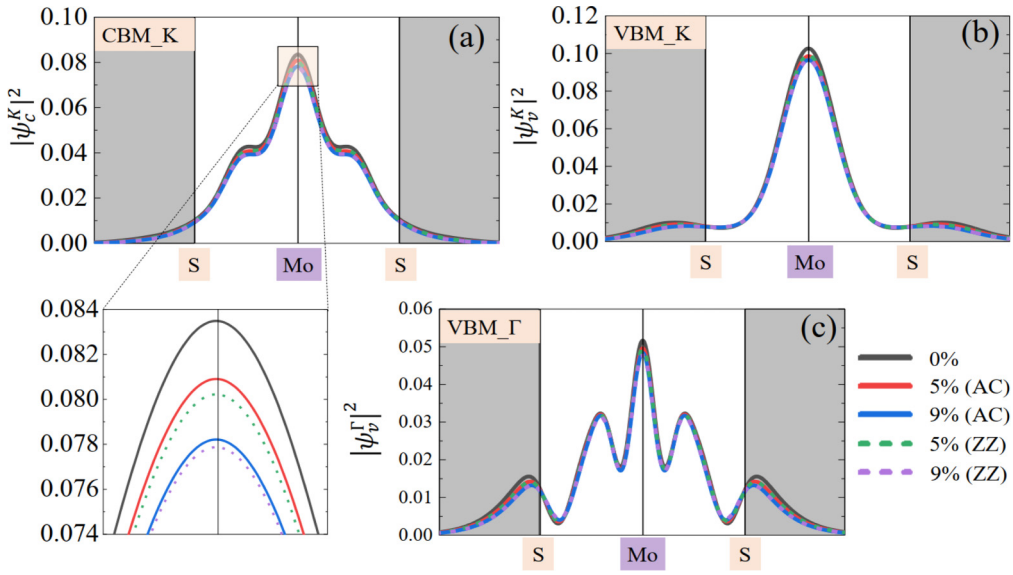

FIG. 6. (a) Spatial distribution of Bloch wave functions at the band edges, CBM (at K), and (b)–(c) VBM at K and Γ, respectively, when strained along the ZZ/AC direction. The planar-average squared wave functions ($|\psi|^2$) have been projected along the direction perpendicular to the basal surface of ML-MoS_2 (width direction). The atomic positions have been marked therein with solid vertical lines on S-Mo-S.

geometry. It strongly affects the low-energy band topology of a strained ML-MoS_2 lattice. In Figs. 5(d) and 5(e), a higher deformation in the orbital charge density distribution is noticed, when strain is along the ZZ direction as compared to the AC direction. The charge density redistribution lead to non-negligible changes in the orbital occupancy that lifts the orbital degeneracy of Bloch states that were initially degenerate for a given electron/hole band at CBM/VBM. The d and p orbitals that are along the strain axis get higher in energy and the orbital wave functions become more stretched along the direction of applied strain. Uniaxial strain-induced orbital motion reduces the orbital overlap between ions, and, in turn, the covalency gets partially reduced with progressive domination of ionicity in the metal-chalcogen bond. As a result, the d bandwidth resulting from the orbital overlap or covalency in the bonds can show a considerable change in the orbital projected density of states (see Fig. S4 of the Supplemental Material [53]).

In Fig. 6, we have shown the spatial profile of Bloch wave functions for relevant band-edge states projected along the direction perpendicular to the MoS_2 surface. Under strain, the stretching of Mo-S bond reduces the probability density of the wave functions, which shows a higher drop when strain is along the ZZ direction.

D. Impact of strain on Berry curvatures

In direct intervalley optical excitations via a circularly polarized light, the optical field only couples to the orbital part of the Bloch wave functions, near the K/K' valleys, while the spin component of carriers remains unaffected during this

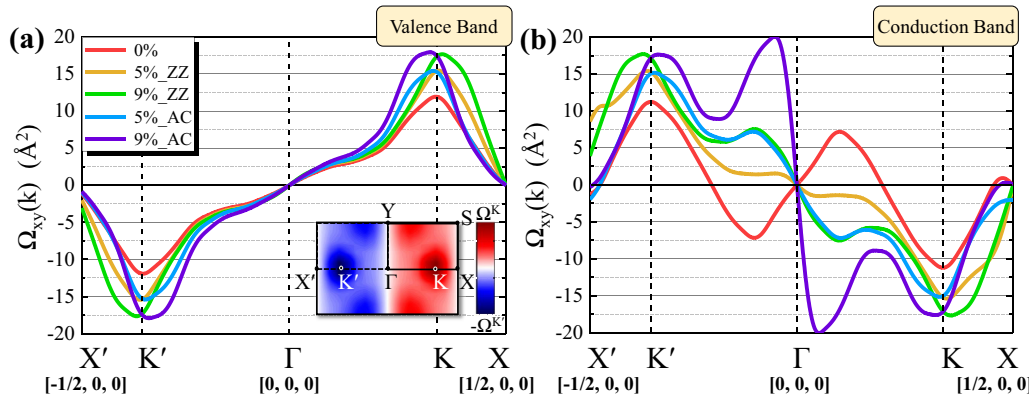

FIG. 7. (a) Berry curvature distribution $\Omega(k)$ over all the occupied Bloch bands in units of $Å^2$ along the high-symmetry k line X'-K'-Γ-K-X, under varying degrees of strain (5%, 9%) along the ZZ/AC direction. (b) Berry curvature distribution of two lowermost unoccupied bands under strain. Inset in (a): contour map of Berry curvature distribution in a 2D k plane for occupied bands.

process. The modification in the onsite electronic energy and orbital occupation factor of a given Bloch state can significantly alter the strength of the Berry curvature distribution of valley carriers that associate valley Hall and spin Hall effects in ML-MoS_2, due to an asymmetric momentum drift in its low-energy Bloch bands [37]. In ML-MoS_2, the degenerate electron/hole bands are energetically indistinguishable around K/K'. But the valley carriers can be identified by their opposite nature of Berry curvature distributions, $\Omega(k)$. In this section, we have studied the effect of a uniaxial tensile deformation on the $\Omega(k)$ of electron/hole bands, near K/K'–points. Figure 7(a) shows the Berry curvatures of all the occupied bands below the Fermi energy for strain-free and strained ML-MoS_2, and Fig. 7(b) represents $\Omega(k)$ for two lowest unoccupied bands along the high-symmetry line X'-K'-Γ-K-X. The lattice inversion symmetry breaking and strong spin-orbit interaction allow charge carriers in these valleys to take opposite spin-polarization and Berry curvatures, where the Berry curvature is mainly localized around the K/K' valleys and significantly peaked at both the K and K' points in the BZ with opposite sign, as required by the time-reversal symmetry of the system. Away from K/K', Ω (k) decays rapidly and eventually vanishes at the Γ point.

When uniaxially strained along the ZZ/AC direction, the intensity profile of $\Omega(k)$ shows a strong drift around K/K', similar to the energy valley drift response in the low-energy Bloch bands. The drift is opposite around K/K', with $\Omega(k)$ crossing K/K' when tensile strain is along the ZZ/AC direction. Importantly, the $\Omega(k)$ distribution is symmetric $[\Omega(-k) = -\Omega(k)]$ about the Γ point along the Γ-X and Γ-X' high-symmetry lines for both unstrained and stained systems. So, the total valley Chern number (C) will be null as the valleys at K/K' follow $C_K = -C_{K'}$, which is expected from a system that respects time-reversal symmetry under strain. However, an increase in $\Omega(k)$ flux intensity together with a drift would affect the dynamics of valley carriers due to a strong coupling between external strain and carriers' valley pseudospin at the band edges that could conveniently alter the valley current (valley Hall conductivity) in uniaxially strained ML-MoS_2, when the system is under an applied transverse electric field. The anomalous transverse velocity gained by the dissociated valley carriers (two different longitudinal charge current polarization for each valley index) could be addressed in a controlled valley-dependent transport experiment where the associated charge carriers are expected to be deflected under an asymmetric strain perturbation [1,67]. To the best of our knowledge, the impact of strain on the Berry curvature distributions $\Omega(k)$ in a strained monolayer MoS_2 has not yet been studied. Herein, we have shown that the strain-induced modification in Bloch states can substantially alter the strength of valley-contrasting phenomena in a strained ML-MoS_2 lattice leading to an anomalous valley current for different Kramer channels that can be mechanically controlled by a strong strain-valley coupling near K and K' points.

E. Strain effect on SOC energy splitting

Since a large strain-field can substantially alter the electronic states around K/K' points, it is worthwhile to address the effect of a uniaxial strain-field in a large strain range of 0–9% on the changes in spin-split valence band maxima (VB1, VB2) and conduction band minima (CB1, CB2) at K/K' points.

In ML-MoS_2, the K/K' valleys are associated with strong spin-orbit coupling (SOC). The absence of lattice inversion symmetry and the presence of frontier Mo $4d$ orbitals lift the spin degeneracy of electronic states near VBM/CBM due to a strong spin-orbit induced spin splitting of bands [60,68]. Figures 8(a)–8(c) show the spin-resolved electronic structure of strain-free (0%) and strained (9%) ML-MoS_2 along the ZZ/AC direction, where the spin projection of carriers is along the out-of-plane spin quantization axis (S_z). Under SOC, electronic states at each valley (K) remain at least twofold Kramer degenerate with those of its entangled time-reversed pair (K'). The spin-split bands at K/K' valleys remain degenerate in electronic energy with opposite spin polarization and crystal momenta in the Brillouin zone, as required by the time-reversal symmetry in the system, with spin index of carriers locked to their valley index, which forms a general basis for coupled spin-valley physics in ML-MoS_2. A pure out-of-plane spin polarization is the result of an interplay of planar electronic confinement of d electrons' motion and the asymmetry in the crystal potential gradient arising from the broken in-plane inversion symmetry [60,69]. A giant spin splitting observed at the VBM, $\sim$149.3 meV, and a relatively small splitting at the CBM, $\sim$3.28 meV, in our DFT calculations show very close agreement with earlier numerical results reported using both the analytical $\mathbf{k}\cdot\mathbf{p}$ Hamiltonian model and *ab initio* calculations [55,68].

In ML-MoS_2, the SOC effects largely arise from the inner orbitals of Mo atoms, and the modification in the geometry of the d orbital wave functions of Bloch electron/holes at the band edges has a sizable effect on the spin-split energies of CBM/VBM under a symmetry-breaking strain, as shown in Fig. 8. A giant spin splitting in the VBM mainly arises from the hybridization between degenerate Mo $4d_{xy}$ and $4d_{x^2-y^2}$ orbitals, where the spatial redistribution of the valley carriers lifts the orbital degeneracy of relevant states under a uniaxial strain by altering their orbital occupancies. This induces a strain-controlled visible splitting in VBM which increases linearly with strain, and reaches $\sim$7 meV at 9% of strain, as indicated in Fig. 8(e), while the CBM of ML-MoS_2 is a result of weak mixing between in-plane S $3p_y + 3p_x$ and out-of-plane Mo $4d_{z^2}$ orbitals. Therefore, the CBM shows a small spin splitting $\sim$1 meV under the application of strain. However, fluctuation in spin splitting at some intermediate strain values is observed in Fig. 8(d). This fluctuation in the spin-split conduction band edge (CBM) could possibly be due to an asymmetric hybridization (i.e., a random spatial overlap) between out-of-plane (Mo $4d_{z^2}$) and in-plane (S $3p_y + 3p_x$) Bloch states on sublattices, which in turn leads to a potential asymmetry around Mo atoms accompanied by the elongation in Mo-S bond. In contrast, the VBM at the Γ point plays no role in spin splitting due to its pure out-of-plane orbitals, S $3p_z$ and Mo $4d_{z^2}$, arising from the crystal symmetry of ML-MoS_2. Occurrence of inversion symmetry along the z direction causes no spin splitting at the Γ point. Since the robustness of valley and spin indexes of valley carriers is closely associated with the carriers' relaxation

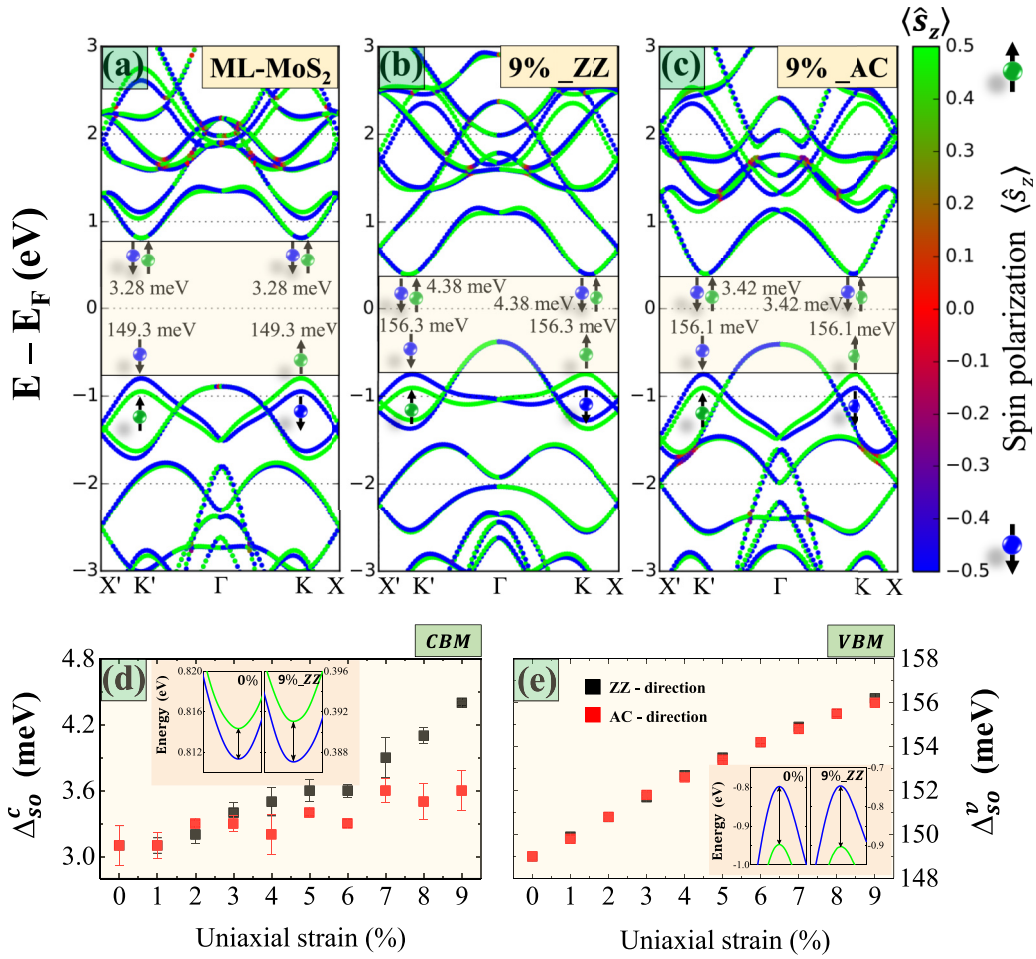

FIG. 8. (a)–(c) Spin-resolved band structure of strain-free (0%) and uniaxially strained (9%) ML-MoS_2 along the ZZ/AC direction. The spin projection is along the out-of-plane spin-projection operator, S_z (dimensionless spin Pauli matrix), and perpendicular to the basal plane of ML-MoS_2. The green and blue colors indicate spin-up and spin-down polarization states. (d) Spin-orbit induced spin splittings of conduction band (CB1, CB2) and (e) valence band (VB1, VB2) under varying degrees of uniaxial strain along the ZZ/AC direction. Insets in (d) and (e) show the CBM and VBM band dispersions for strain-free (0%) and 9% strained cases along the ZZ direction.

time, an increase in the SOC energy difference in hole bands (∼7 meV) can hold the spin orientations of carriers for a longer time and the hole relaxation is expected to be slower due to the suppression of Dyakonov-Perel spin relaxation [70].

In ML-MoS_2, the direct interband optical transitions from a spin-split valence band (VB1, VB2) to the conduction band (CB1, CB2), at the *K* point, give rise to strongly bound A and B excitons, with optical selection rules maintaining spin conservation of valley carriers [29,59,68]. A strong spin-strain coupling in a strained ML-MoS_2 is expected to widen the energy separation between A and B excitons leading to a strain tunable exciton splitting under a large strain field (0–9%). Experiments on ML-MoS_2 shows the ability of ML-MoS_2 to withstand a sufficiently large elastic strain field as high as 6% to 11% without undergoing any mechanical failure [20]. Therefore, SOC spin splitting at the VBM/CBM can be considered carefully in studies pertaining to large strain engineering in MoS_2, where the spin degrees of freedom of valley carriers can be manipulated simply by controlling the spatial distribution of their Bloch orbitals.

IV. CONCLUSIONS

In summary, using first-principles calculations, we have shown the impact of a symmetry reducing mechanical deformation on the low-energy carrier dynamics in strained ML-MoS_2, around *K*/*K*' points. We find a strong strain-valley coupling for low-energy valley carriers, where the energy extrema of electron/hole bands drift away from *K*/*K*' points in response to a symmetry lowering uniaxial strain. A large valley asymmetry between electron and hole states (i.e., the CBM valley drift is nearly 2 times that of the VBM hills) can conveniently lift the valley symmetry (valley momentum degeneracy at *K*/*K*') of electrons/holes. The resulting effect considerably influences the valley selective optical excitations and valley polarization properties in a multivalley electronic system like ML-MoS_2. A drastic drop in the degree of circular polarization (*K* valley polarization) can be optically addressed by a polar PL emission measurement [37]. Besides, the *K*-valley coherence effect can manipulate the valley-contrasting Berry curvature distributions around *K*/*K*', where the rise in flux profile together with a drift can lead to anomalous

valley current in strained ML-MoS_2 [1]. This strong valley asymmetry between valley carriers under a directional lattice strain is the interplay of geometric and orbital overlap effects that breaks the lattice symmetry and symmetry between orbital wave functions at the relevant band-edge points. The profundity in our electronic structure calculations is validated as follows. The band gap is found to remain direct close to 2% of uniaxial tensile strain under the effects of SOC, which closely agrees with experimentally observed direct-to-indirect band-gap transition occurring at a critical strain value of ∼2%. The redshift rate in the direct band gap, $E_g(K\text{-}K) \sim 51$–$53\,\mathrm{meV/strain\%}$ under uniaxial strain, shows a very good agreement with earlier experimental reports: 35 meV/(1% strain) [62], 45 ± 7 meV/% [17], and 48 meV/% [37] observed in optical absorption and photoluminescence (PL) spectroscopy. Moreover, the rate of the redshift of the indirect band gap, $E_g(\Gamma\text{-}K) \sim 100\,\mathrm{meV/\%}$, is in good accord with the theoretical value, 94.6 ± 2.2 meV/% [61] under uniaxial tensile strain. Moreover, the spatial redistribution and rehybridization of states near the band edges can potentially pave the way to controlling the spin degrees of freedom in a uniaxially strained ML-MoS_2, where the spin-orbit coupling (SOC) induced spin-splitting energy at the VBM can be sizably enlarged by an amount of 7 meV at a strain of 9%. This could potentially alter the spintronic capability of this material and allow manipulating the spin degrees of freedom in a strained MoS_2 lattice. The spin relaxation times of carriers are expected to be prolonged by the suppression of Dyakonov-Perel spin relaxation due a strain-induced increase in the spin-splitting energy. The theoretical findings in this report may drive further experimental investigations of ML-MoS_2 under the application of in-plane lattice strain to realize its future technological applications.

Note added. Recently, a combined experimental and theoretical study by Son *et al.* [67] on the Berry curvature dipole in a strained monolayer MoS_2 has been published. We were not aware of this publication, which is close to our current work and yet a bit different. However, only one kind of strain, namely, uniaxial, was considered by Son *et al.* in their theoretical calculations, in support of the experimental results. Nevertheless, all kinds of in-plane strain have been investigated in our detailed work, which also differs from that of Son *et al.* in the range and magnitude of strain studied.

ACKNOWLEDGMENTS

We extend our sincere thanks to the Centre for Development of Advanced Computing (C-DAC), Pune for providing its supercomputing facility on PARAM YUVA II and the Institute of Nano Science and Technology, Mohali for infrastructural and fellowship support. We thank Dr. Seema Arora for helpful discussions related to this work. M.K.M. acknowledges support via a Ph.D. fellowship and Grant No. 09/1129(0007)/2017-EMR-I from the Council of Scientific and Industrial Research (CSIR), India. Financial support provided by Grant No. SR/NM/NS-1125/2016 from the Department of Science and Technology (Nanomission), Government of India is gratefully acknowledged by A.D.S.

[1] D. Xiao, G. B. Liu, W. Feng, X. Xu, and W. Yao, Phys. Rev. Lett. **108**, 196802 (2012).
[2] M. Chhowalla, H. S. Shin, G. Eda, L.-J. Li, K. P. Loh, and H. Zhang, Nat. Chem. **5**, 263 (2013).
[3] K. F. Mak, C. Lee, J. Hone, J. Shan, and T. F. Heinz, Phys. Rev. Lett. **105**, 136805 (2010).
[4] K. K. Kam and B. A. Parkinson, J. Phys. Chem. **86**, 463 (1982).
[5] A. Kuc, N. Zibouche, and T. Heine, Phys. Rev. B **83**, 245213 (2011).
[6] H. Zeng, J. Dai, W. Yao, D. Xiao, and X. Cui, Nat. Nanotechnol. **7**, 490 (2012).
[7] T. Cao, G. Wang, W. Han, H. Ye, C. Zhu, J. Shi, Q. Niu, P. Tan, E. Wang, B. Liu, and J. Feng, Nat. Commun. **3**, 885 (2012).
[8] K. F. Mak, K. He, J. Shan, and T. F. Heinz, Nat. Nanotechnol. **7**, 494 (2012).
[9] B. Radisavljevic, A. Radenovic, J. Brivio, V. Giacometti, and A. Kis, Nat Nano **6**, 147 (2011).
[10] S. Mohammad Tabatabaei, M. Noei, K. Khaliji, M. Pourfath, and M. Fathipour, J. Appl. Phys. **113**, 163708 (2013).
[11] J. Feng, X. Qian, C.-W. Huang, and J. Li, Nat. Photonics **6**, 866 (2012).
[12] H. Shi, H. Pan, Y. W. Zhang, and B. I. Yakobson, Phys. Rev. B **87**, 155304 (2013).
[13] H. Peelaers and C. G. Van de Walle, Phys. Rev. B **86**, 241401(R) (2012).
[14] D. Fu, J. Zhou, S. Tongay, K. Liu, W. Fan, T.-J. King Liu, and J. Wu, Appl. Phys. Lett. **103**, 183105 (2013).
[15] M. Hosseini, M. Elahi, M. Pourfath, and D. Esseni, J. Phys. D: Appl. Phys. **48**, 375104 (2015).
[16] S. Yu, H. D. Xiong, K. Eshun, H. Yuan, and Q. Li, Appl. Surf. Sci. **325**, 27 (2015).
[17] H. J. Conley, B. Wang, J. I. Ziegler, R. F. Haglund Jr., S. T. Pantelides, and K. I. Bolotin, Nano Lett. **13**, 3626 (2013).
[18] A. Castellanos-Gomez, M. Poot, G. A. Steele, H. S. J. Van Der Zant, N. Agraït, and G. Rubio-Bollinger, Adv. Mater. **24**, 772 (2012).
[19] A. Castellanos-Gomez, M. Poot, G. A. Steele, H. S. J. van der Zant, N. Agrait, and G. Rubio-Bollinger, Nanoscale Res. Lett. **7**, 233 (2012).
[20] S. Bertolazzi, J. Brivio, and A. Kis, ACS Nano **5**, 9703 (2011).
[21] C. Lee, X. Wei, J. W. Kysar, and J. Hone, Science **321**, 385 (2008).
[22] C. Gómez-Navarro, M. Burghard, and K. Kern, Nano Lett. **8**, 2045 (2008).
[23] Q. Yue, J. Kang, Z. Shao, X. Zhang, S. Chang, G. Wang, S. Qin, and J. Li, Phys. Lett. A **376**, 1166 (2012).
[24] N. Jena, S. D. Behere, and A. De Sarkar, J. Phys. Chem. C **121**, 9181 (2017).
[25] R. C. Cooper, C. Lee, C. A. Marianetti, X. Wei, J. Hone, and J. W. Kysar, Phys. Rev. B **87**, 035423 (2013).
[26] N. Zibouche, P. Philipsen, A. Kuc, and T. Heine, Phys. Rev. B **90**, 125440 (2014).
[27] A. Ramasubramaniam, D. Naveh, and E. Towe, Phys. Rev. B **84**, 205325 (2011).

[28] Y. Wang, C. Cong, C. Qiu, and T. Yu, Small **9**, 2857 (2013).
[29] K. He, C. Poole, K. F. Mak, and J. Shan, Nano Lett. **13**, 2931 (2013).
[30] A. Castellanos-Gomez, R. Roldán, E. Cappelluti, M. Buscema, F. Guinea, H. S.J. van der Zant, and G. A. Steele, Nano Lett. **13**, 5361 (2013).
[31] C. Si, Z. Sun, and F. Liu, Nanoscale **8**, 3207 (2016).
[32] W. Wei, Y. Dai, and B. Huang, Phys. Chem. Chem. Phys. **19**, 663 (2016).
[33] M. Ghorbani-Asl, S. Borini, A. Kuc, and T. Heine, Phys. Rev. B **87**, 235434 (2013).
[34] G. Sallen, L. Bouet, X. Marie, G. Wang, C. R. Zhu, W. P. Han, Y. Lu, P. H. Tan, T. Amand, B. L. Liu, and B. Urbaszek, Phys. Rev. B **86**, 081301(R) (2012).
[35] D. Xiao, M.-C. Chang, and Q. Niu, Rev. Mod. Phys. **82**, 1959 (2010).
[36] K. Kośmider, J. W. González, and J. Fernández-Rossier, Phys. Rev. B **88**, 245436 (2013).
[37] C. R. Zhu, G. Wang, B. L. Liu, X. Marie, X. F. Qiao, X. Zhang, X. X. Wu, H. Fan, P. H. Tan, T. Amand, and B. Urbaszek, Phys. Rev. B **88**, 121301(R) (2013).
[38] O. Gunawan, Y. P. Shkolnikov, K. Vakili, T. Gokmen, E. P. De Poortere, and M. Shayegan, Phys. Rev. Lett. **97**, 186404 (2006).
[39] G. Kresse and D. Joubert, Phys. Rev. B **59**, 1758 (1999).
[40] P. E. Blöchl, Phys. Rev. B **50**, 17953 (1994).
[41] G. Kresse and J. Hafner, Phys. Rev. B **48**, 13115 (1993).
[42] G. Kresse and J. Hafner, Phys. Rev. B **49**, 14251 (1994).
[43] G. Kresse and J. Furthmüller, Phys. Rev. B **54**, 11169 (1996).
[44] J. P. Perdew, K. Burke, and M. Ernzerhof, Phys. Rev. Lett. **77**, 3865 (1996).
[45] J. P. Perdew and Y. Wang, Phys. Rev. B **45**, 13244 (1992).
[46] T. Fukui, Y. Hatsugai, and H. Suzuki, J. Phys. Soc. Japan **74**, 1674 (2005).
[47] Y. Cai, G. Zhang, and Y.-W. Zhang, J. Am. Chem. Soc. **136**, 6269 (2014).
[48] J. Xiao, M. Q. Long, M. J. Li, X. M. Li, H. Xu, and K. S. Chan, Phys. Chem. Chem. Phys. **17**, 6865 (2015).
[49] T.-T. Jia, M.-M. Zheng, X.-Y. Fan, Y. Su, S.-J. Li, H.-Y. Liu, G. Chen, and Y. Kawazoe, Sci. Rep. **6**, 18869 (2016).
[50] Y. Su and X. Fan, Chinese Phys. B **26**, 108101 (2017).
[51] W. S. Yun, S. W. Han, S. C. Hong, I. G. Kim, and J. D. Lee, Phys. Rev. B **85**, 033305 (2012).
[52] Y. Liang, S. Huang, R. Soklaski, and L. Yang, Appl. Phys. Lett. **103**, 042106 (2013).
[53] See Supplemental Material at http://link.aps.org/supplemental/10.1103/PhysRevB.100.165413 for the continuous evolution of SOC band structure and zoomed section of VBM/CBM from 0–10% strain in Fig. S1; band structure under uniaxial compressive strain in Fig. S2; band-edge valley drift for shear (S_1 and S_2) strain and biaxial strain in Fig. S3; and atom and orbital projected partial density of states in Fig. S4.
[54] M. Mohr, K. Papagelis, J. Maultzsch, and C. Thomsen, Phys. Rev. B **80**, 205410 (2009).
[55] A. Kormányos, V. Zólyomi, N. D. Drummond, P. Rakyta, G. Burkard, and V. I. Fal'ko, Phys. Rev. B **88**, 045416 (2013).
[56] D. Dimple, N. Jena, A. Rawat, and A. De Sarkar, J. Mater. Chem. A **5**, 22265 (2017).
[57] M. A. Cazalilla, H. Ochoa, and F. Guinea, Phys. Rev. Lett. **113**, 077201 (2014).
[58] F. Guinea, M. I. Katsnelson and A. K. Geim, Nat. Phys. **6**, 30 (2010).
[59] A. Ramasubramaniam, Phys. Rev. B **86**, 115409 (2012).
[60] Z. Y. Zhu, Y. C. Cheng, and U. Schwingenschlögl, Phys. Rev. B **84**, 153402 (2011).
[61] T. Li, Phys. Rev. B **85**, 235407 (2012).
[62] L. Yang, X. Cui, J. Zhang, K. Wang, M. Shen, S. Zeng, S. A. Dayeh, L. Feng, and B. Xiang, Sci. Rep. **4**, 5649 (2014).
[63] Q. Zhang, Y. Cheng, L.-Y. Gan, and U. Schwingenschlögl, Phys. Rev. B **88**, 245447 (2013).
[64] P. Johari and V. B. Shenoy, ACS Nano **6**, 5449 (2012).
[65] J. Wiktor and A. Pasquarello, Phys. Rev. B **94**, 245411 (2016).
[66] N. L. Heda, A. Dashora, A. Marwal, Y. Sharma, S. K. Srivastava, G. Ahmed, R. Jain, and B. L. Ahuja, J. Phys. Chem. Solids **71**, 187 (2010).
[67] J. Son, K-H Kim, Y. H. Ahn, H-W Lee, and Jieun Lee, Phys. Rev. Lett. **123**, 036806 (2019).
[68] T. Cheiwchanchamnangij and W. R. L. Lambrecht, Phys. Rev. B **85**, 205302 (2012).
[69] N. Alidoust, G. Bian, S.-Y. Xu, R. Sankar, M. Neupane, C. Liu, I. Belopolski, D.-X. Qu, J. D. Denlinger, and F.-C. Chou, Nat. Commun. **5**, 4673 (2014).
[70] Z. Wang, A. Molina-Sánchez, P. Altmann, D. Sangalli, D. De Fazio, G. Soavi, U. Sassi, F. Bottegoni, F. Ciccacci, M. Finazzi, L. Wirtz, A. C. Ferrari, A. Marini, G. Cerullo, and S. Dal Conte, Nano Lett. **18**, 6882 (2018).